inorganics

MDPI

Article

Three-Dimensional Ternary rGO/VS_2/WS_2 Composite Hydrogel for Supercapacitor Applications

Sahil S. Magdum, Sadhasivam Thangarasu * and Tae Hwan Oh *

School of Chemical Engineering, Yeungnam University, Gyeongsan 38541, Republic of Korea
* Correspondence: sadhasivam.nano@gmail.com (S.T.); taehwanoh@ynu.ac.kr (T.H.O.)

Abstract: In recent years, the development of lightweight electrode materials with excellent performance (energy density versus power density) has increased the number of uses for supercapacitors. Creating three-dimensional skeletal network structures with excellent specific capacitance and high energy density is still challenging. This study utilized a straightforward one-pot hydrothermal technique to construct a supercapacitor based on hydrogel 3D skeletal networks comprising rGO nanosheets with VS_2/WS_2 nanoparticles. The rGO appeared as flakes and layers, interconnected in nature, allowing for more ion transport pathways and a larger active surface area for EDLC performance. The heterostructured VS_2 and WS_2 nanoparticles were homogeneously anchored to the rGO layers and were porous in the hydrogel structure. The functioning rGO, rGO-VS_2, and rGO-VS_2-WS_2 composite hydrogel electrodes were created without a binder on the Ni foam current collector using a hydraulic press. The rGO-VS_2-WS_2 composite hydrogel electrode showed excellent supercapacitor performance of 220 F g^{-1} at 1 A g^{-1} in 3M KOH electrolyte, which was more than those of the GO (158 F g^{-1}) and rGO-VS_2 (199 F g^{-1}) hydrogels under similar conditions. Hydrogel electrodes made of rGO-VS_2-WS_2 had a power density of 355 Whkg^{-1} and a high energy density of 30.55 Whkg^{-1}. It maintained a high energy density of up to 21.11 W/kg^{-1}, even at a high power density of 3454 W/kg^{-1}. Given the 3D shape and the excellent surface properties of rGO nanosheets with VS_2 and WS_2 nanoparticles as the hydrogel, this electrode has essential properties that make it a good choice for making high-performance capacitors.

Keywords: reduced graphene oxide; vanadium disulfide; tungsten disulfide; hydrogel; binder-free electrode; supercapacitor

Citation: Magdum, S.S.; Thangarasu, S.; Oh, T.H. Three-Dimensional Ternary rGO/VS_2/WS_2 Composite Hydrogel for Supercapacitor Applications. *Inorganics* **2022**, *10*, 229. https://doi.org/10.3390/inorganics10120229

Academic Editors: Faxing Wang and Tao Wang

Received: 30 September 2022
Accepted: 24 November 2022
Published: 28 November 2022

1. Introduction

Clean, renewable energy sources have drawn rising interest in combating the depletion of conventional fossil fuels and global warming [1–3]. Among different energy storage technologies [4–7], supercapacitors (SCs) attract considerable attention because of their excellent electrochemical characteristics, such as rapid charge and discharge rates, a high specific power density, and excellent cycle stability [8–13]. To address the need for high capacitance in supercapacitors, novel approaches have recently focused on various structured, dimensional, and combinational electrode materials [14–16]. As an example, Zheng et al. used the mechanically induced sol–gel transition method to prepare chitin-based activated carbon (ACNC-800) with a high nitrogen content (7.1%) for supercapacitor electrodes. The electrochemical analysis was done using the three-electrode electrochemical system in NaOH medium. As a result, the achieved specific capacitance of (ACNC-800) was 245 F/g at 0.5 A/g. The increased surface area of the interconnected porous framework (ACNC-800) is the main reason for achieving high performance [17]. A simple, one-step co-pyrolysis method was used for preparing the N-doped hierarchical porous carbon (HPC) materials from biomass, and that prepared material was used as a supercapacitor electrode material. Urea-prepared HPC electrode obtains an excellent specific capacitance of 300 F/g at 1 A/g and an energy density of 14.3 Wh kg^{-1} [18]. Cao et al. used phytic acid treatment for

as-prepared P-doped and wood-derived carbon. The symmetrical supercapacitor device attained high specific capacitance of 206.5 F g^{-1} at a current density 1.0 mA cm^{-2} [19]. For supercapacitors, flax-based porous carbon was impregnated with $ZnCl_2$ and activated at high temperatures. The electrode materials were used to obtain the specific capacitance of 105 F/g at a 1 A/g current density. In another report, N-doped and S-doped pollen-derived graphene provided an interconnected "sphere-in-layer" structure of electrode materials [20]. N-doped and S-doped pollen-derived graphene electrodes displayed specific capacitance of 420 F/g at 1 A/g. To avoid aggregation of the graphene sheet, the pollen-derived carbon sphere was represented as a porous spacer in the composite [21]. Guo et al. used a direct one-pot polymerization technique to prepare the Mn-ion-doped polylevodopa synthetic melanin nanoparticles and transformed them into tiny hybrid carbon nanoparticles. MnO distributed MnO@CNPs electrode materials provided excellent specific capacitance of 545 F/g at 0.5 A/g in 6 M KOH electrolyte [22].

To further extend the advantages of electrode materials, the hydrogels may be employed as efficient supercapacitor electrode materials due to their thick nanostructured matrix, high specific surface area, and enhanced electrical performance [23]. Hydrogel development is a feasible technique where several conductive elements can be included in the colloidal gel porous networks. Along with good electrochemical performances, such as more power density, good capacitance retention, and high conductivity, most colloidal gels have exceptional mechanical and physical characteristics, like light weight, biocompatibility, and the ability to stretch, twist, and fold [24]. Transition metal dichalcogenides (TMDs) have caught the attention of many scientists because of their unique layered structure and properties. This means that they could be used in fields like energy conversion, energy storage, field-effect transistors, and catalysis. TMDs, like VS_2, MoS_2, and WS_2, have drawn significant interest recently due to their distinctive layered architectures, more efficient electrical conductivity, and higher active sites. In this, vanadium disulfide (VS_2) has been considered an efficient pseudocapacitive component due to its high conductivity, interlayer spacing, and structural phenomena [25–27]. Furthermore, theoretical research has also shown that a single layer of VS2 is metallic, which makes it easier for charge transfer [28,29]. Similarly, WS_2 can be prepared as a multi-layer or single-layer TMD, where the band gap of WS_2 varies based on the arrangements of layers [30–34]. WS_2 comprises squeezed S-W-S layers that assemble along the carbon axis and are held together by van der Waals forces. The metallic W atom has an electrovalent bond with six S neighbors [35,36]. The sequential structure and hybridization of WS_2 with graphene would have synergistic effects depending on the amount of WS_2. The optimal amount of WS_2 in the capacitor shows excellent cyclic stability, high specific capacitance, and good rate capability. For example, Bhat et al. [37] suggested that making hybrid samples from carbon-based material is a second tactic to improve electrochemical performance. Graphene is one of the most sought-after carbon compounds. Its volume increase during charging and discharging has been taken care of by processes that have made materials better at conducting electrons and ions and staying stable during cycling. This is because graphene has a large specific surface area, excellent electrical conductivity, good mechanical properties, and exceptional strength [38]. In some cases, graphene-based products develop unsustainable stacking, which causes them to have a lower specific surface area and lower capacitive performance. The low capacitance may be caused by a reduction in the place where the electric double layer forms at the interface [39]. Several ideas for creating connected 3D graphene structure have been developed to stop the stacking of graphene sheets, again like hydrogels. The specific capacitance values of the graphene hydrogel and MnO_2-graphene hydrogel electrodes were determined to be 113 and 200.6 F g^{-1} at a current volume of 1 A [40]. Graphene oxide has been assembled in aqueous environments using a variety of reduction agents or crosslinkers to produce reduced graphene oxide hydrogels, which are dried before being utilized as electrode materials. Surface-crumpled graphene hydrogels with macro- and microporous architectures were developed by Chaoyang et al. for ultrahigh-volumetric energy storage [37]. Kim and colleagues used a reliable open-porosity nanostructure in

an interfacial layer-by-layer self-assembled graphene nanoribbon hydrogel (GNH). The edge-abundant property of GNH is useful for extra nitrogen functionalization, improving the performance of supercapacitors [41]. Graphene hydrogels were also employed as active components, such as metal oxide/sulfide or a conductive polymer, to make hybrids free of a binder and self-standing. Hong Zhong Chi et al. reported that the manganese oxide/graphene hydrogel produced by positing electrodes exhibited a specific capacitance of 352.9 F g^{-1} at 1 A g^{-1} [42]. Due to the open-porosity and highly conductive graphene hydrogel network, active compounds with high redox activity and high specific capacitance are found in these hybrid-based supercapacitors, which show high specific capacitance and high cycle stability. The reduced form of graphene oxide and the hybrid hydrogel also worked well as supercapacitor. For example, Yuxi Xu et al. created a self-assembled graphene hydrogel (SGH). In an aqueous electrolyte, the SGH demonstrated reasonable specific capacitance (175 F/g) as a 3D supercapacitor electrode material. Using a reduced graphene oxide (rGO) hydrogel, a high-energy-density symmetric supercapacitor has been developed, where 539 F/g (rGOH-50) specific capacitance can be attained in the active electrolyte at a discharge current density of 1 A/g [38].

In the present study, a binary composite of rGO/VS_2 hydrogel was designed and fabricated through a hydrothermal method and freeze-drying process. The efficient amount of rGO/VS_2 was optimized by using different concentrations of rGO and VS_2, named rG-V-1, rG-V-2, rG-V-3, and rG-V-4 composites. The hydrogels were prepared as binder-free electrodes. Among the various ratios in binary (rGO/VS_2) hydrogels, the resultant rG-V-1 hydrogel has a large specific capacitance, high energy/power density, and outstanding rate performance. We made a ternary composite hydrogel called rG-V-W-1 and rG-V-W-2 by mixing WS_2 with rGO/VS_2 (as rGO/VS_2/WS_2). We did this using the simple hydrothermal method and the freeze-drying process. The electrode materials' structural, microstructural, and electrochemical properties were characterized and confirmed using microscopic, spectroscopic, and electrochemical techniques.

2. Experimental Section

2.1. Chemicals

Sulfuric acid (H_2SO_4, ~95%), potassium permanganate ($KMnO_4$, ~99.3%), hydrogen peroxide (H_2O_2, 30%), orthophosphoric acid (H_3PO_4, 98%), sodium tungstate dihydrate ($H_4Na_2O_6W$, 98–101%), ethanol (EtOH, 94.5%), and potassium hydroxide (KOH, >85%) were obtained from Duksan Chemicals and Metals, the Republic of Korea. Ammonium metavanadate (ACS reagent) was obtained from Acros Organics. Thioacetamide (C_2H_5NS, GR Grade) was purchased from Duksan pure chemicals Co. Ltd., Republic of Korea. Ethylenediamine (>99%) and hydrazine hydrate (N_2H_4 50–60%) was purchased from Sigma-Aldrich. The graphite flakes (Alfa Aesar), ammonia (NH_3, 28%, Junsei), and DI water were used for this study. Nickel foam was purchased from NARA Cell-Tech Corporation.

2.2. Synthesis of Graphene Oxide and Preparation of Vanadium Disulfide (VS_2)

Hummer's method was modified to prepare graphene oxide (GO) [43]. Typically, 180 mL of H_2SO_4 and 20 mL of H_3PO_4 were mixed in a beaker in a 9:1 ratio and 1.50 g of ball-milled graphite flakes were added while the mixture was constantly stirred. Then, 9.0 g of $KMnO_4$ was added and the water bath was maintained at 50 °C for 12 h. The ice cubes were prepared by mixing 200 mL of DI water with 1.5% of 30% H_2O_2, and the resulting solution was applied to them. The GO-containing solution was dried at room temperature after being repeatedly centrifuged with DI water and ethanol at 10,000 rpm to achieve a pH of nearly 7. The hydrothermal process was used to prepare the VS_2 nanoparticles [44]. Usually, to dissolve ammonium metavanadate, 30 mL of purified water and 6 mL of ammonia are used (0.47 g). Thioacetamide (1.5 g) was added to the solution after the ammonium metavanadate had completely dissolved while being stirred magnetically. A 30 min vigorous stirring process produced a yellow-black fluid. This solution was put into a Teflon-walled 50 mL stainless steel autoclave. The autoclave was preheated to 180 °C and

then kept there for 20 h. The autoclave was then cooled. The black product was repeatedly cleaned with ethanol and deionized water. The obtained product was given the designation VS_2 nanoparticles after being dried for 12 h in a vacuum air oven at 60 °C.

2.3. Development of rGO Hydrogels

Ethylene diamine was used as a cross-linker in the hydrothermal process to make the rGO hydrogel [38]. Firstly, 40 mL of graphene oxide dispersion (40 mL DI water + 200 mg GO) was sonicated for 20 min to prepare the rGO hydrogels. Ethylene diamine was added to the mixture after 117.5 µL of ethylene, and the mixture was agitated for 10 min. A 50 mL Teflon-lined autoclave with the solution inside was transferred and preheated for 12 h at 180 °C. After the autoclave had cooled to room temperature, the rGO hydrogel was made and washed many times in deionized water. The surface characteristics of the rGO hydrogel were changed by a chemical diminution in 15 mL of 50% hydrazine hydrate for 6 h at 50 °C. This altered the surface characteristics of the rGO hydrogels. The hydrogels were cleaned in deionized water for two days after they had been at room temperature for two days.

2.4. Binary Composite Hydrogel (rGO-VS_2 (rG-V)) Preparation

Using anhydrous ethylene diamine as a cross-linker during a hydrothermal process, a reduced graphene oxide/vanadium sulfide (rGO-VS_2) composite hydrogel was synthesized. Four different concentrations were prepared. For preparing the binary composite, the desired amount of vanadium disulfide (10, 25, 35, or 45 mg) was dispersed into 20 mL of graphene oxide (90, 75, 65, and 55 mg) using sonication for 20 min. Afterward, 58 µL of ethylene diamine was added to the dispersion and stirred for 10 min. Finally, the mixture was heated to 180 °C for 12 h in a 50 mL Teflon-lined autoclave. After the autoclave had naturally cooled to room temperature, the rG-V hydrogel was produced and cleaned by submerging it in deionized water multiple times. Chemical reduction in 50% hydrazine hydrate was used to alter the surface characteristics of the rG-V hydrogel for 6 h at 50 °C. The hydrogel was then frozen and dried for 24 h. The four concentrations of VS_2 (10, 25, 35, or 45 mg) were named rG-V-1, rG-V-2, rG-V-3, and rG-V-4 hydrogels, respectively.

2.5. Preparation of rG-V-W Hydrogel

For preparing the ternary hydrogel, the VS_2/WS_2 composite was designed in two ways. Firstly, ammonium metavanadate (0.47 g) was mixed with of 30 mL of distilled water and 6 mL of ammonia. Afterwards, 0.3 g of $Na_2WO_4.2H_2O$ and 1.8 g of thioacetamide were added to the solution and stirred vigorously for 30 min. Then, the hydrothermal reaction was carried out in a 50 mL Teflon-lined stainless-steel reactor. The reaction took place at 180 °C for 20 h. After reaching room temperature, the material was rinsed with DI water and ethanol several times. Finally, as-prepared VS_2-WS_2 composite materials were dried at 60 °C for 10 h in vacuum oven and the as-prepared material denoted as V-W-1. In another way, VS_2 was initially prepared as mentioned in the Section 2.2. Then, the above similar procedure was followed to prepare the VS_2-WS_2 composite by using VS_2 instead of ammonium metavanadate and named as V-W-2. Figure 1 shows the synthesis of the rG-V-W-1 hydrogel. As is typical, 0.01 g of as-prepared VS_2/WS_2 (VW-1) was included in 20 mL of graphene oxide solution and it was effectively dispersed via sonication for 15 min. After sonication, 58 µL of ethylene diamine was added to the mixture and agitated for 10 min. This mixed solution was transferred to a 50 mL Teflon-lined autoclave. Then it was heated to 180 °C for 12 h. The rGO/VW-1 hydrogel (abbreviated rG-V-W-1) was produced and cleaned by submerging it in deionized water multiple times after the autoclave had naturally cooled to room temperature. Chemical reduction in 30 mL of hydrazine hydrate (50%) was used to alter the surface characteristics of the rG-V-W-1 hydrogel for 6 h at 50 °C. The hydrogel was then frozen and dried for 24 h. The same procedure was used to prepare the rG-V-W-2 using V-W-2.

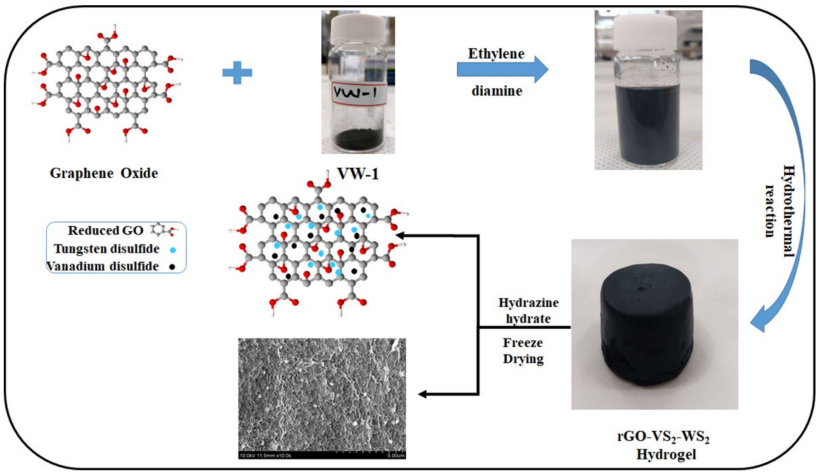

Figure 1. Schematic illustration of the synthesis procedure for ternary composite hydrogels.

2.6. Structural/Microstructural Characterization and Electrochemical Measurements

The functional group of the as-prepared materials was confirmed using an FT–IR spectrometer (Perkin Elmer spectrum 100, USA). The crystalline properties of the materials were confirmed through X-ray diffraction (XRD, Xpert Pro) equipped with Cu Kα. The chemical composition of materials was analyzed using Raman spectroscopy (XploRA plus, HORIBA Jobin Yuon S.A.S, France). The surface microstructures, particle size, elemental composition, and mapping were analyzed through field emission-scanning electron microscopy (FE-SEM HITACHI S-4800 equipped with EDAX, Japan) and transmission electron microscopy (BIO-TEM HITACHI H-7600, Japan). The electrochemical performances were assessed using a three-electrode setup using Corrtest (CS350 in COM3) electrochemical workstation. Before applying hydrogel, nickel foam (Ni-foam, 1 × 1 cm) was pretreated with 100 mL of 3 M HCL, deionized water, and ethanol. Finally, the treated Ni-foam stayed dry overnight at 70 °C. The platinum plate, Hg/HgO, and active material compressed in Ni foam was employed for electrochemical experiments as the counter electrode, reference electrode, and working electrode, respectively. For this study, the electrolyte solution was 3 M KOH. For electrochemical measurements, approximately 2.0 mg of synthesized hydrogel was hydraulically pressed (10 pa for 30 s) onto nickel foam to prepare the working electrode without using a binder. To determine cyclic voltammetry (CV), analysis was carried out (0 to −1 V) at various scan rates (5, 10, 20, 50, and 100 mV/s). Galvanostatic charge–discharge (GCD) analysis was done to determine the specific capacitances of the electrodes at different current densities. The electrochemical impedance spectroscopy (EIS) measurement was carried out in the frequency range of 100,000 to 0.01 kHz at an amplitude of 5 mV.

3. Results and Discussion

The FTIR analysis was carried out to confirm the formation and surface functional properties of the as-prepared materials. The obtained FT-IR data of GO are represented in Figure 2a. For GO, a broader peak was attained between 2906 to 3565 cm^{-1}, which is a part of the OH group's strong extending mode [45]. In Figure 2b, GO peaked at 1734 cm^{-1}, showing the extending modes of C=O. Moreover, the absorption peak was reached at 1623 cm^{-1} due to the C=C extending mode. The peak at 1056 cm^{-1} is related to the extending modes of the (C−O) [45]. The FTIR results confirmed that the synthesis of GO from the graphite was successful. The FTIR spectra of rGO hydrogels showed absorption peaks at around 1041, 1397, 1999, 2903, and 2984 cm^{-1}, which were all consistent with the C−O−C and C−OH extending vibration, skeletal vibration of the graphitic skeleton, CH_2 extending vibration, and OH extending vibration, respectively. Moreover, the hydroxyl peak mostly disappeared in rGO. This indicates that GO nanosheets were reduced during the hydrothermal reaction. When GO is changed into rGO, it can change

the way electricity flows during electrochemical performances. In the case of rGO-VS_2, the peak at 884 cm^{-1} corresponds to the S stretches of ν(V=S) terminal, which confirms the existence of the V^{4+} oxidation state in VS_2. For the rGO/VS_2/WS_2 hydrogel, the band at 640 cm^{-1} could be related to the W–S bonds and S–S bonds of WS_2. These results have confirmed the deposition of WS_2 on rGO nanosheet surfaces [46,47]. In addition to the previously indicated, VS_2 peaks were found with WS_2 on rGO. The Raman spectra of the ternary hydrogel are shown in Figure S1. Two major peaks in Raman spectra of the rG-V-W-1 at 1355 cm^{-1} and 1599 cm^{-1} are attributable to D and G bands for carbon materials, respectively. Figure 2b displays the powder XRD patterns of the rGO, rGO/VS_2-1, and rGO/VS_2/WS_2 hydrogels. The XRD patterns in Figure 2b for the freeze-dried rGO showed a broad peak with a center angle of 2θ = 24.82°. Peak intensity for the 24.82° diffraction peak was greater for rGO reduced by hydrazine than GO. It can be seen that the large diffraction peaks of the pure rGO hydrogel indicate that all GO was converted into rGO with much-reduced functionality [48]. In the XRD patterns of the rG-V-1 composite hydrogel, the diffraction peaks at 2θ of 15.04, 35.46, and 57.34°are attributed to reflections from (001), (011), and (103), confirming the formation and presence of VS_2 (JCPDS No. 89-1640) with the rGO. The peaks of VS_2 in VS_2-rGO agreed with the hexagonal phase [49–51]. In the rGO-VS_2-WS_2 composite hydrogel XRD patterns, WS_2 showed two diffraction peaks at 2θ = 15.16° and 43.94° which are located on the (002) and (106) planes of hexagonal WS_2 (JCPDS No. 01-087-2417) [52], respectively. Moreover, the diffraction peaks of VS_2 coexisted with WS_2 at their corresponding locations, confirming the efficient formation of the rGO-VS_2-WS_2 composite hydrogel and anchoring the VS_2 and WS_2 nanoparticles in the hydrogel structure.

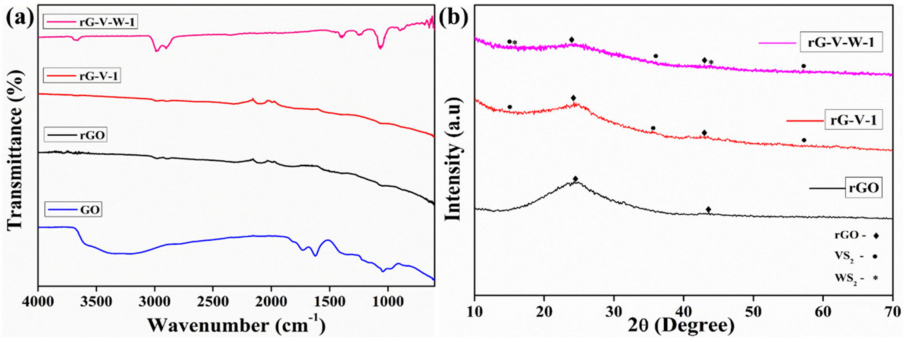

Figure 2. (**a**) Fourier-transform infrared spectroscopy spectra of GO, rGO, rG−V−1, and rG−V−W-1. (**b**) The X-ray diffraction patterns for the rGO, rG−V−1, and rG−V−W−1.

SEM micrograph analysis was performed to recognize the microstructural properties of the different hydrogels. Figure 3 represents the SEM images of pure rGO hydrogel and rG-V-1 hydrogel. In the pure rGO hydrogel (Figure 3a), a D structure of graphene with sustainable macropores in the micrometer size range is seen in a porous state. The rGO looked like flakes and layers that were connected and porous. This gives more ways for ions to move through the material and a more active surface area for EDLC. In addition, each rGO layer looked thin. The thin layer of the rGO provided different diameters of pores during the interconnection between each thin layer. This phenomenon offers a lighter density for rGO-based hydrogels. Figure 3b,c show that a 3D porous network structure has been made for the rG-V-1 composite hydrogel. In this case, it has been seen that VS_2 nanoparticles stick to graphene nanosheets in a uniform way. Notably, the formation of rGO hydrogel was not affected by incorporating VS_2 in the hydrogel during the binary composite development. Figure 3d–h shows the results of an EDAX investigation to further assess the VS_2 nanoparticles' ability to adhere to the graphene nanosheets. As shown in the EDAX spectra (Figure 3e), the major peaks related to carbon (C), vanadium (V), and sulfur (S), which proved that the hydrogel was composed of rGO and VS_2 using linkers. The elemental maps of the C, S, and V analyses of the composite hydrogel were obtained

to understand how the VS_2 nanoparticles were distributed within the 3D graphene-based framework. It was likely confirmed that VS_2 had distributed uniformly across the 3D porous frameworks. SEM and EDAX investigations were carried out on the rGO-VS_2 with WS_2 to determine the impact and dispersion of two kinds of VS_2 and WS_2 materials on the hydrogel network structure. The resulting images are shown in Figure 4. TMDs like VS_2 and WS_2 nanoparticles can be effectively dispersed in the rGO sheet-like structure [53]. Figure 4a–c indicates that the nano-sized particles were distributed uniformly throughout the layered structure. Moreover, the particles effectively adhered to the surface and the pores in the hydrogel. The unanticipated agglomeration of rGO sheets can be successfully prevented by including VS_2 and WS_2 in the rGO layers, where the nanoparticles can act as spacers between graphene sheets. Based on these characteristics, increases in the material's specific surface area and enhanced permeability of electrolyte ions can be obtained, which will eventually enhance EDLC performance. As shown in the EDAX spectra (Figure 4e), the hydrogel of the composite was mainly made of C, V, S, and tungsten (W). This proves that the VS_2 and WS_2 nanoparticles were on the rGO layers at some point. To further examine the homogeneity of rGO, VS_2, and WS_2, EDAX mapping analyses were performed (Figure 4f–i). For rGO-VS_2-WS_2 composite hydrogel, the elements C, V, S, W, and C were obtained. Further, it confirms the homogeneity of VS_2 and WS_2 in rGO-based ternary hydrogels. The TEM images of the highly dispersed rG-V-W-1 hydrogel material are shown the Figure S3. They reveal that the VS_2/WS_2 nanomaterials were effectively anchored on the surface of the rGO.

Initially, the electrochemical performances of hydrogels (rGO and rG-V-1, rG-V-2, rG-V-3, and rG-V-4) were measured through cyclic voltammetry (CV), galvanostatic charge–discharge (GCD), and electrochemical impedance spectroscopy (EIS) characteristics in an electrode configuration with 3 M KOH electrolyte solution. We measured the electrochemical performance by loading 2.2 mg of rGO, 1.3 mg of rG-V-1, 2.3 mg of rG-V-2, 1.8 mg of rG-V-3, and 2.0 mg of rG-V-4 composite hydrogels separately into the Ni foam. We aimed to load a similar mass of electrode materials onto the Ni foam for each hydrogel. During the process of making electrodes, the hydraulic press caused an unexpected loss of active materials. Thus, we could use different amounts of electrode materials for each electrode. The electrochemical performances were determined based on the mass of electrode materials, and the results are provided in Figures 5–7. Figure 5a–e displays the CV curves of rGO and rG-V-1, rG-V-2, rG-V-3, and rG-V-4 composite hydrogels, respectively. The CV analysis was captured at different scan speeds, varying from 5 to 100 mV/s (specifically at 5, 10, 20, 50, and 100 mV/s). The CV curves of rGO and rG-V-1, rG-V-2, rG-V-3, and rG-V-4 composite hydrogel electrodes showed rectangular-shaped hysteresis loops. All of the EDLCs had rectangular CV curves, which were demonstrated mainly by the way the rGO hydrogels behaved in terms of their high surface area and porosity. The interconnected network of rGO flake hydrogel and its higher porosity are great for ion diffusion and may offer more sites for charge adsorption, which makes EDLC work well. The area of the curve in the composite hydrogel material is greater/inferior to that of the pristine rGO due to the presence of VS_2. In the presence of VS_2, the surface properties of the hydrogel may be altered, which may alter the charge adsorption sites in the material. It is evident that compared to rGO, rG-V-2, rG-V-3, and rG-V-4 hydrogel electrodes, the rG-V-1 composite hydrogel electrode possesses a wider area than the other composites, which may indicate a higher specific capacitance. Moreover, the rectangular shape has no discernible distortion at higher scan rates. Figure 6a–e shows the GCD curves for rGO, rG-V-1, rG-V-2, rG-V-3, and rG-V-4 composite hydrogel electrodes, respectively. The CGD measurements were carried out in the voltage range of -1.0 to 0.0 V at different current densities (1, 2, 3, 5, and 10 A/g). In all cases, linear curves in the voltage range depict a double-layer capacitor's ideal performance. Moreover, efficient charge and discharge characteristics have been observed in the hydrogels. Charge and discharge times vary based on the mass of the material. Comparatively, excellent charge and discharge performances were obtained from the rG-V-1. To determine the supercapacitor properties of each electrode material,

the specific capacitance was calculated based on the GCD performance and mass of the active materials.

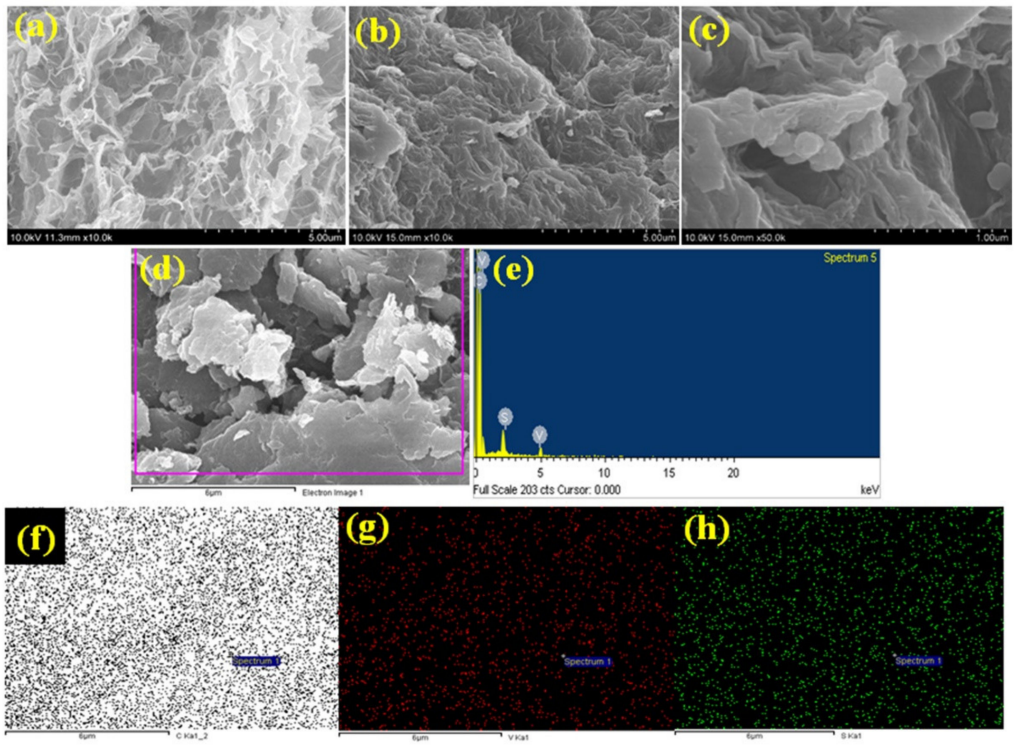

Figure 3. Scanning electron microscopy micrograph images, (**a**) rGO and (**b**,**c**) rG-V-1. (**d**–**h**) Energy dispersive X-ray analysis results of rG-V-1. EDAX mapping of (**f**) carbon, (**g**) vanadium, and (**h**) sulfur.

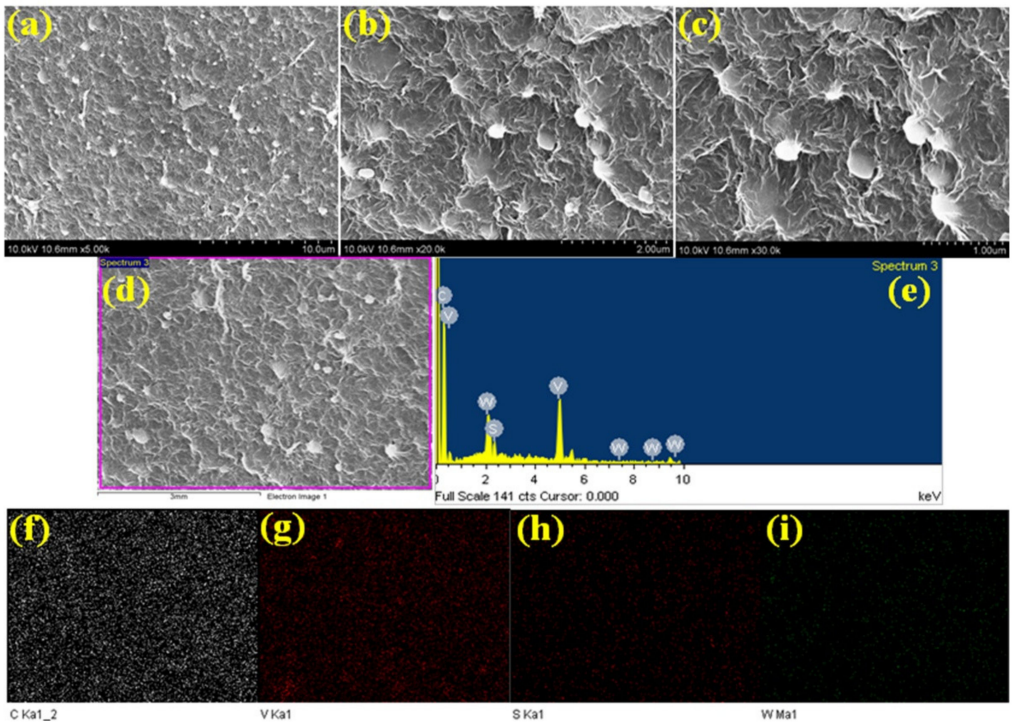

Figure 4. (**a**–**d**) Lower and higher magnification scanning electron microscopy micrograph images of rG-V-W-1. (**e**) EDAX spectra of rG-V-W-1. EDAX mapping data of (**f**) carbon, (**g**) vanadium, (**h**) sulfur, and (**i**) tungsten.

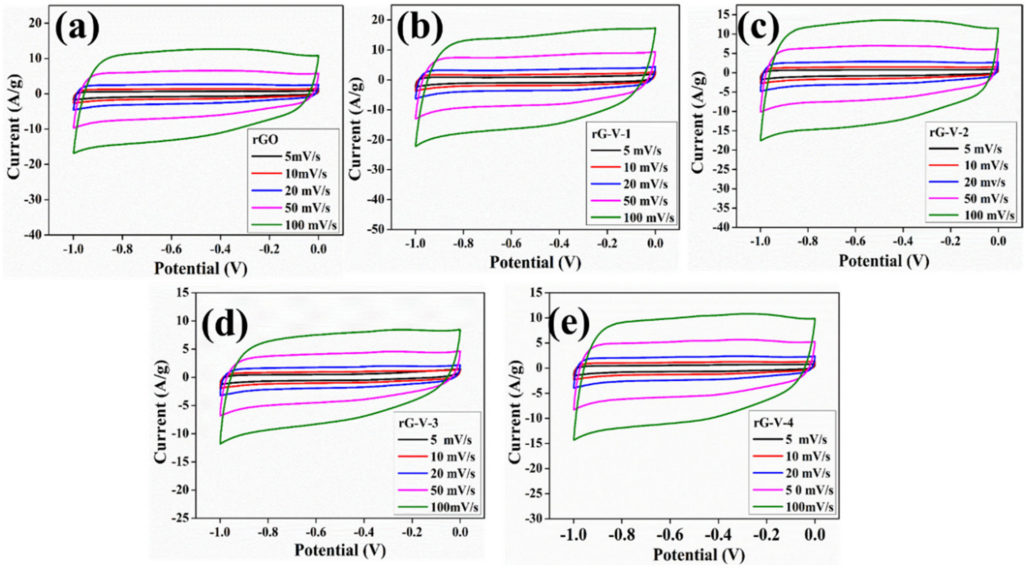

Figure 5. Cyclic voltammetry curves of (**a**) rGO (**b**) rG−V−1, (**c**) rG−V−2 (**d**) rG−V−3, and (**e**) rG−V−4 at different scan rates.

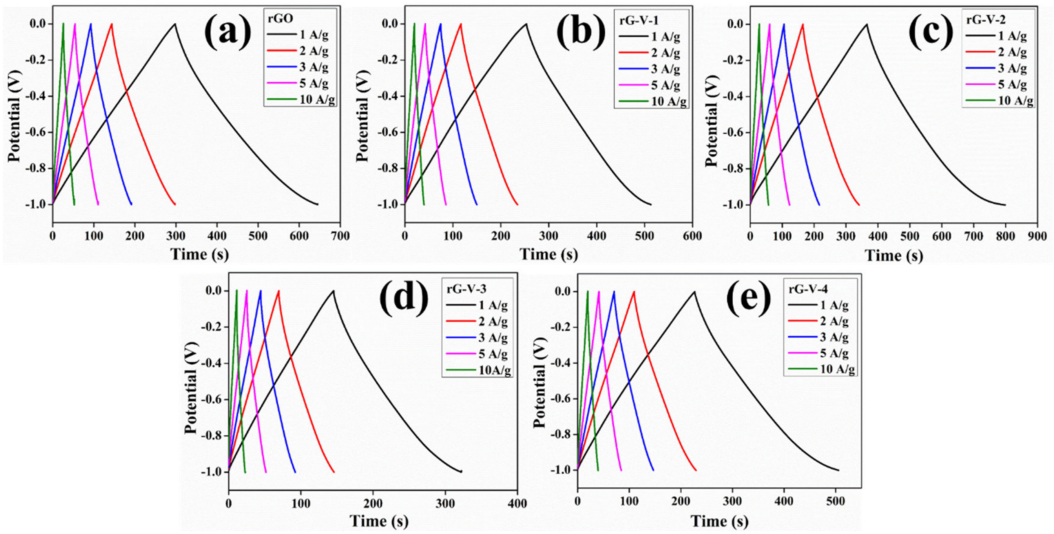

Figure 6. Galvanostatic charge/discharge curves of (**a**) rGO (**b**) rG−V−1, (**c**) rG−V−2 (**d**) rG−V−3, and (**e**) rG−V−4 at different current densities.

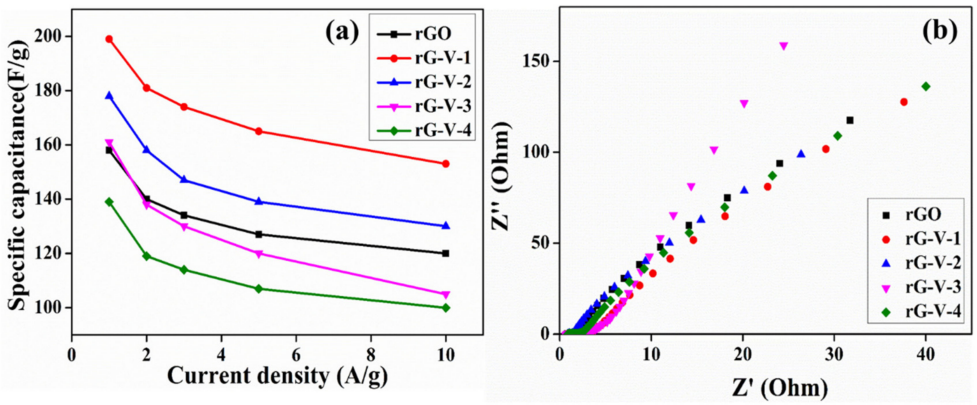

Figure 7. (**a**) Specific capacitance curves and (**b**) electrochemical impedance spectroscopy analysis of rGO, rG-V-1, rG-V-2, rG-V-3, and rG-V-4.

The specific capacitance of different hydrogels at different current densities in a three-electrode system is illustrated in Figure 7a. The specific capacitance (C_s) of the electrode materials was calculated according to the following formula:

$$C_s = (I\Delta t)/(m\Delta V)$$

where I is current, m is the mass of the materials, Δt is discharge time, and ΔV is potential window [54]. At a current density of 1 A/g, the rGO hydrogel was found to have a specific capacitance of 158 F/g. As the current density increased, the specific capacitance of rGO hydrogel slowly decreased. At 1, 2, 3, 5, and 10 A/g, the specific capacitances were 158, 140, 134, 127, and 120 F/g, respectively. Composite hydrogel electrodes (rG-V-1, rG-V-2, rG-V-3, and rG-V-4) were also shown to behave similarly. By introducing VS_2 in the hydrogel, the specific capacitance of the rGO was significantly altered (Figure 7a). The specific capacitance of rGO at 1 A/g was found to be 158 F/g, while the specific capacitance of rG-V-1, rG-V-2, rG-V-3, and rG-V-4 at the same current density was 199, 178, 161, and 139 F/g, respectively. The rG-V-1 composite hydrogel electrodes had the highest specific capacitance compared to the rGO, rG-V-1, rG-V-3, and rG-V-4 hydrogel electrodes. The EIS analysis was further used to determine the properties of electrodes. The Nyquist plots of rGO and binary composite hydrogels are shown in Figure 7b. The R_{ct} of the hydrogel electrode showed a similar response as a straight line, which is consistent with the electrode and electrolyte interface of ion diffusion in the high-frequency zone [55]. The strong assembly and the beneficial interactions between the VS_2 nanoparticles and rGO sheets are credited with the outstanding charge transfer performance of the rG-V-1 electrode. The interconnectivity and accessibility of the porous structure of VS_2/rGO make it possible for faster electrolyte ion diffusion and faster adsorption kinetics. This also makes the electrochemical properties better.

To further improve the supercapacitor performance of the rGO-VS_2 composite hydrogel, the WS_2 nanoparticles were jointly developed with VS_2 in the rGO hydrogel. The CV and GCD performances were performed on two kinds of rGO-VS_2-WS_2 composite hydrogel (denoted as rG-V-W-1 and rG-V-W-2 hydrogel), and the corresponding results are shown in Figure 8. To determine the supercapacitor performances, the mass of 1.7 mg for rG-V-W-1 and 2.1 mg for rG-V-W-2 were used. For the rG-V-W-1 and rG-V-W-2 hydrogels (Figure 8a,b), the CV curves showed a rectangular nature at varied scan rates, demonstrating their EDLC-like behavior. Compared to the rG-V-W-2 hydrogel, the CV curve area of the rG-V-W-1 hydrogel electrode was more extensive, which led us to conclude that the rG-V-W-1 attained a higher specific capacitance performance. The CGD performances of rG-V-W-1 and rG-V-W-2 composite hydrogels were determined at different current densities (1, 2, 3, 5, and 10 A/g) in the potential window of -1.0 to 0.0 V, and the resulting data are shown in Figure 8c,d. Based on the amount of active material in the electrode and under the same conditions, the rG-V-W-1 has shown better charge and discharge performance than the rG-V-W-2. The specific capacitance was computed using the charge/discharge curves at various discharge currents. The specific capacitance values for the hydrogels rG-V-W-1 and rG-V-W-2 are shown in Figure 9a. Figure 9a shows that the rG-V-W-1 electrode had a maximum capacitance of 220 F/g at 1 A/g. In contrast, the rG-V-W-2 electrode exhibited a specific capacitance of 179 F/g. We saw a drop in capacitance at higher current densities and scan rates. This is because charged ions do not move around as much at higher scan rates. In the literature, similar effects have been reported for supercapacitors built from hybrid carbon-based materials [56]. The EIS characteristic curves of rG-V-W-1 and rG-V-W-2 are shown in Figure 9b. The rG-V-W-1 hydrogel electrode was significantly smaller than other materials due to its improved surface compatibility. Figure 9c demonstrates the power density vs. energy density information of the rG-V-W-1 and rG-V-W-2 composite hydrogel electrodes. Remarkably, rG-V-W-1 hydrogel electrodes delivered a high energy density of 30.55 Wh kg^{-1}, with a power density of 355 Wkg^{-1}. Even at a high power density of 3454 W kg^{-1}, it maintained a high energy density of up to 21.11 Whkg^{-1}. For the rG-V-W-2 hydrogel, lower energy and power density have been obtained under similar

conditions. At a power density of 223 Wkg^{-1}, the rG-V-W-2 hydrogel electrodes provided a high energy density of 24.86 W h kg^{-1}. Moreover, it maintained a high energy density of up to 18.61 W h kg^{-1}, even at a high power density of 2233 W kg^{-1}. However, the performance of rG-V-W-2 hydrogel was inferior to the rG-V-W-1 composite hydrogel electrodes. The high electrical conductivity of the composite and the uniform coverage of WS_2 and VS_2 nanoparticles on rGO sheets enhanced the electrochemical use of VS_2 and WS_2 and sped up the transit of the electrolyte ions in charge of the superior capacitive performance of the rG-V-W-1 composite hydrogel electrode.

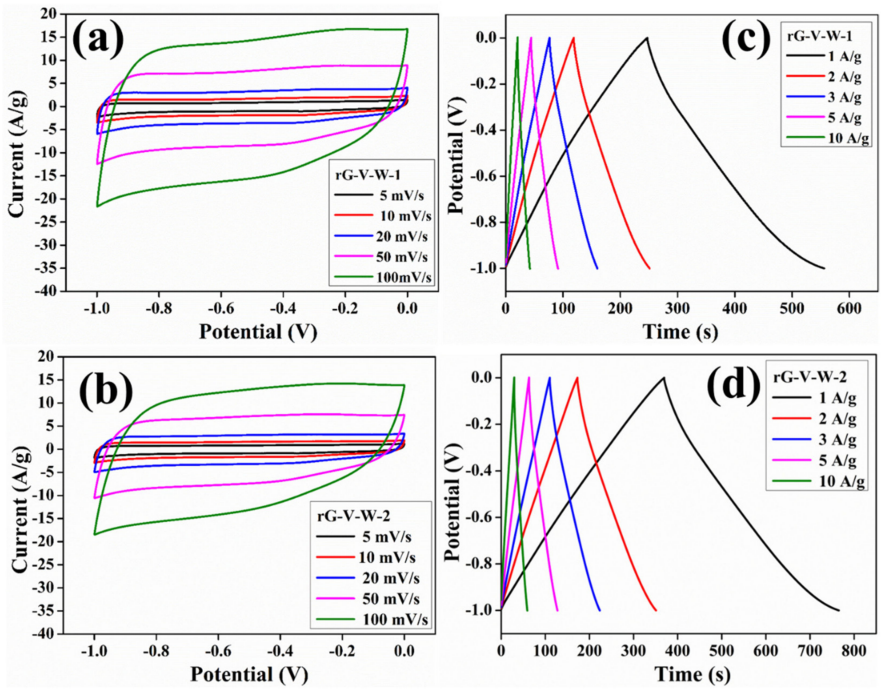

Figure 8. Cyclic voltammetry curves of (**a**) rG−V−W−1 and (**b**) rG−V−W−2 at different scan rates. Galvanostatic charge/discharge (GCD) curves of (**c**) rG−V−W−1 and (**d**) rG−V−W−2 at different current densities.

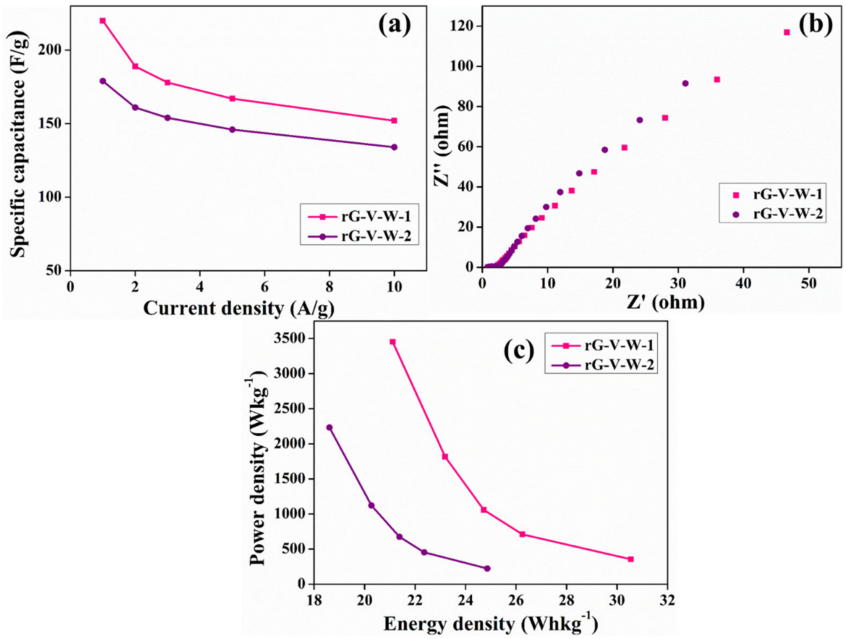

Figure 9. (**a**) Specific capacitance curves, (**b**) electrochemical impedance spectroscopy data and (**c**) Ragone plots of rG-V-W-1 and rG-V-W-2.

4. Conclusions

In conclusion, supercapacitor electrode materials based on hydrogels made of rGO nanosheets with VS_2 and WS_2 nanoparticles as 3D skeleton networks were effectively synthesized. We successfully deposited the hydrogel materials' high surface area with excellent porosity characteristics on the current collectors for estimating supercapacitor performances. Initially, a different ratio of rGO nanosheets and VS_2 nanoparticles (as rG-V-1, rG-V-2, rG-V-3, and rG-V-4) was prepared, and the excellent concentration was optimized based on electrochemical performances. Electrochemical properties could be controlled reasonably well because the VS_2 nanoparticles were firmly attached to the rGO nanosheets and spread out evenly. The rG-V-1 hydrogel exhibited excellent electrochemical characteristics, including a greater specific capacitance of 199 F/g at 1 A/g, which was higher than that of the rGO and other binary hydrogels. WS_2 was added to rGO-VS_2-WS_2 as a ternary component to tune the electrochemical performance, specifically the specific capacitance properties of rGO-VS_2. The rGO-VS_2-WS_2 hydrogel exhibited the highest performance (220 F/g at 1 A/g). Additionally, the rGO-VS_2-WS_2 had an outstanding energy density of 30.55 $Whkg^{-1}$ with a power density of 355 Wkg^{-1}. The excellent capacitive performance in rGO-VS_2-WS_2 was possibly attained as a result of the increased electrical conductivity of the composite and the uniform coverage of VS_2 and WS_2 nanoparticles on rGO sheets. These factors also made it easier for electrolytes to move quickly and increase the electrochemical utilization of WS_2 and VS_2. The enhanced electrochemical properties of the rGO-VS_2-WS_2 hydrogel may be used in high-performance supercapacitors.

Supplementary Materials: The following supporting information can be downloaded at: https://www.mdpi.com/article/10.3390/inorganics10120229/s1, Figure S1: Raman spectra of the rG-V-W-1 hydrogel; Figure S2. XRD of VS2, WS2 and rG-V-4. Figure S3: Transmission Electron Microscopy images of the rG-V-W-1 hydrogel.

Author Contributions: Conceptualization, S.S.M., S.T. and T.H.O.; methodology, S.S.M. and S.T.; validation, S.T. and T.H.O.; formal analysis, S.S.M.; investigation, S.S.M.; resources, T.H.O.; data curation, S.S.M. and S.T; writing—original draft preparation, S.S.M.; writing—review and editing, S.T. and T.H.O.; supervision, S.T. and T.H.O.; project administration, T.H.O.; funding acquisition, T.H.O. All authors have read and agreed to the published version of the manuscript.

Funding: This research was supported by Yeungnam University research grants in 2022.

Institutional Review Board Statement: Not applicable.

Informed Consent Statement: Not applicable.

Data Availability Statement: Not applicable.

Conflicts of Interest: The authors declare no conflict of interest.

References

1. Ren, J.; Luo, Q.; Hou, Q.; Chen, H.; Liu, T.; He, H.; Wang, J.; Shao, Q.; Dong, M.; Wu, S.; et al. Suppressing Charge Recombination and Ultraviolet Light Degradation of Perovskite Solar Cells Using Silicon Oxide Passivation. *ChemElectroChem* **2019**, *6*, 3167–3174. [CrossRef]
2. Yin, H.; Zhang, X.; Lu, J.; Geng, X.; Wan, Y.; Wu, M.; Yang, P. Substrate effects on the CVD growth of MoS2 and WS2. *J. Mater. Sci.* **2019**, *55*, 990–996. [CrossRef]
3. Liu, M.; Meng, Q.; Yang, Z.; Zhao, X.; Liu, T. Ultra-long-term cycling stability of an integrated carbon–sulfur membrane with dual shuttle-inhibiting layers of graphene "nets" and a porous carbon skin. *Chem. Commun.* **2018**, *54*, 5090–5093. [CrossRef] [PubMed]
4. Wang, Z.; Qin, J.; Hu, Q.; Wang, D.; Wang, F.; Zhong, Y.; Zhang, J.; Zhou, H.; Dong, M.; Hu, C. Theoretical investigation of molybdenum/tungsten-vanadium solid solution alloy membranes: Thermodynamic stability and hydrogen permeation. *J. Membr. Sci.* **2020**, *608*, 118200. [CrossRef]
5. Wei, H.G.; Wang, H.; Li, A.; Cui, D.P.; Zhao, Z.N.; Chu, L.Q.; Wei, X.; Wang, L.; Pan, D.; Fan, J.C.; et al. Multifunctions of Polymer Nanocomposites: Environmental Remediation, Electromagnetic Interference Shielding, And Sensing Applications. *ChemNanoMat* **2020**, *6*, 174–184. [CrossRef]
6. Zhang, K.; Wang, H.; Su, W.; Wang, T.; Wang, X.; Chen, T.; Huo, T.; Dang, F.; Dong, M.; Wang, C.; et al. Trace bismuth and iodine co-doping enhanced thermoelectric performance of PbTe alloys. *J. Phys. D Appl. Phys.* **2020**, *53*, 245501. [CrossRef]

7. Tan, J.; Li, D.; Liu, Y.; Zhang, P.; Qu, Z.; Yan, Y.; Hu, H.; Cheng, H.; Zhang, J.; Dong, M. A self-supported 3D aerogel network lithium–sulfur battery cathode: Sulfur spheres wrapped with phosphorus doped graphene and bridged with carbon nanofibers. *J. Mater. Chem. A* **2020**, *8*, 7980–7990. [CrossRef]
8. Li, X.; Zhao, W.; Yin, R.; Huang, L.; Qian, X. A highly porous polyaniline-graphene composite used for electrochemical supercapacitors. *Eng. Sci.* **2018**, *3*, 89–95. [CrossRef]
9. Dong, H.; Li, Y.; Chai, H.; Cao, Y.; Chen, X. Hydrothermal Synthesis of CuCo S Nano-structure and N-Doped Graphene for High-2 4 Performance Aqueous Asymmetric Supercapacitors. *ES Energy Environ.* **2019**, *4*, 19–26. [CrossRef]
10. Ma, Y.; Ma, M.; Yin, X.; Shao, Q.; Lu, N.; Feng, Y.; Lu, Y.; Wujcik, E.K.; Mai, X.; Wang, C.; et al. Tuning polyaniline nanostructures via end group substitutions and their morphology dependent electrochemical performances. *Polymer* **2018**, *156*, 128–135. [CrossRef]
11. Yang, L.; Guo, X.; Jin, Z.; Guo, W.; Duan, G.; Liu, X.; Li, Y. Emergence of melanin-inspired supercapacitors. *Nano Today* **2021**, *37*, 101075. [CrossRef]
12. Wang, Y.; Zhang, L.; Hou, H.; Xu, W.; Duan, G.; He, S.; Liu, K.; Jiang, S. Recent progress in carbon-based materials for supercapacitor electrodes: A review. *J. Mater. Sci.* **2021**, *56*, 173–200. [CrossRef]
13. Duan, G.; Zhao, L.; Zhang, C.; Chen, L.; Zhang, Q.; Liu, K.; Wang, F. Pyrolysis of zinc salt-treated flax fiber: Hierarchically porous carbon electrode for supercapacitor. *Diam. Relat. Mater.* **2022**, *129*, 109339. [CrossRef]
14. Zhang, X.; Zhang, J.; Chen, Y.; Cheng, K.; Yan, J.; Zhu, K.; Ye, K.; Wang, G.; Zhou, L.; Cao, D. Freestanding 3D Polypyrrole@ reduced graphene oxide hydrogels as binder-free electrode materials for flexible asymmetric supercapacitors. *J. Colloid Interface Sci.* **2019**, *536*, 291–299. [CrossRef] [PubMed]
15. Wei, H.; Wang, H.; Li, A.; Li, H.; Cui, D.; Dong, M.; Lin, J.; Fan, J.; Zhang, J.; Hou, H. Advanced porous hierarchical activated carbon derived from agricultural wastes toward high performance supercapacitors. *J. Alloy. Compd.* **2020**, *820*, 153111. [CrossRef]
16. Shang, Y.; Zhang, J.; Xu, L.; Liu, H.; Zhou, B.; Tang, Y.; Zhu, L.; Jiang, X.; Jiang, X. Facile synthesis of a graphene/nickel-cobalt hydroxide ternary hydrogel for high-performance supercapacitors. *J. Colloid Interface Sci.* **2018**, *531*, 593–601. [CrossRef]
17. Zheng, S.; Zhang, J.; Deng, H.; Du, Y.; Shi, X. Chitin derived nitrogen-doped porous carbons with ultrahigh specific surface area and tailored hierarchical porosity for high performance supercapacitors. *J. Bioresour. Bioprod.* **2021**, *6*, 142–151. [CrossRef]
18. Cao, L.; Li, H.; Xu, Z.; Zhang, H.; Ding, L.; Wang, S.; Zhang, G.; Hou, H.; Xu, W.; Yang, F.; et al. Comparison of the heteroatoms-doped biomass-derived carbon prepared by one-step nitrogen-containing activator for high performance supercapacitor. *Diam. Relat. Mater.* **2021**, *114*, 108316. [CrossRef]
19. Wang, F.; Cheong, J.Y.; He, Q.; Duan, G.; He, S.; Zhang, L.; Zhao, Y.; Kim, I.-D.; Jiang, S. Phosphorus-doped thick carbon electrode for high-energy density and long-life supercapacitors. *Chem. Eng. J.* **2021**, *414*, 128767. [CrossRef]
20. Duan, G.; Zhao, L.; Chen, L.; Wang, F.; He, S.; Jiang, S.; Zhang, Q. ZnCl 2 regulated flax-based porous carbon fibers for supercapacitors with good cycling stability. *New J. Chem.* **2021**, *45*, 22602–22609. [CrossRef]
21. Cao, L.; Li, H.; Liu, X.; Liu, S.; Zhang, L.; Xu, W.; Yang, H.; Hou, H.; He, S.; Zhao, Y. Nitrogen, sulfur co-doped hierarchical carbon encapsulated in graphene with "sphere-in-layer" interconnection for high-performance supercapacitor. *J. Colloid Interface Sci.* **2021**, *599*, 443–452. [CrossRef]
22. Guo, W.; Guo, X.; Yang, L.; Wang, T.; Zhang, M.; Duan, G.; Liu, X.; Li, Y. Synthetic melanin facilitates MnO supercapacitors with high specific capacitance and wide operation potential window. *Polymer* **2021**, *235*, 124276. [CrossRef]
23. Han, X.; Xiao, G.; Wang, Y.; Chen, X.; Duan, G.; Wu, Y.; Gong, X.; Wang, H. Design and fabrication of conductive polymer hydrogels and their applications in flexible supercapacitors. *J. Mater. Chem. A* **2020**, *8*, 23059–23095. [CrossRef]
24. Wang, F.; Jiang, C.; Tang, C.; Bi, S.; Wang, Q.; Du, D.; Song, J. High output nano-energy cell with piezoelectric nanogenerator and porous supercapacitor dual functions—A technique to provide sustaining power by harvesting intermittent mechanical energy from surroundings. *Nano Energy* **2016**, *21*, 209–216. [CrossRef]
25. EMeyer, E.; Bede, A.; Mutukwa, D.; Taziwa, R.; Zingwe, N. Optimization, and analysis of carbon supported VS2 nanocomposites as potential electrodes in supercapacitors. *J. Energy Storage* **2019**, *27*, 101074.
26. Murugan, A.V.; Quintin, M.; Delville, M.-H.; Campet, G.; Vijayamohanan, K. Entrapment of poly (3, 4-ethylenedioxythiophene) between VS 2 layers to form a new organic–inorganic intercalative nanocomposite. *J. Mater. Chem. A* **2005**, *15*, 902–909. [CrossRef]
27. Huang, Z.; Han, X.; Cui, X.; He, C.; Zhang, J.; Wang, X.; Lin, Z.; Yang, Y. Vertically aligned VS 2 on graphene as a 3D heteroarchitectured anode material with capacitance-dominated lithium storage. *J. Mater. Chem. A* **2020**, *8*, 5882–5889. [CrossRef]
28. Torad, N.L.; Hu, M.; Kamachi, Y.; Takai, K.; Imura, M.; Naito, M.; Yamauchi, Y. Facile synthesis of nanoporous carbons with controlled particle sizes by direct carbonization of monodispersed ZIF-8 crystals. *Chem. Commun.* **2013**, *49*, 2521–2523. [CrossRef]
29. Pang, S.; Tsao, H.N.; Feng, X.; Müllen, K. Patterned graphene electrodes from solution-processed graphite oxide films for organic field-effect transistors. *Adv. Mater.* **2009**, *21*, 3488–3491. [CrossRef]
30. Li, N.; Su, J.; Xu, Z.; Li, D.-P.; Liu, Z.-T. Theoretical and experimental investigation on structural and electronic properties of Al/O/Al, O-doped WS 2. *J. Phys. Chem. Solids* **2016**, *89*, 84–88. [CrossRef]
31. Abbas, O.A.; Lewis, A.H.; Aspiotis, N.; Huang, C.-C.; Zeimpekis, I.; Hewak, D.W.; Sazio, P.; Mailis, S. Laser printed two-dimensional transition metal dichalcogenides. *Sci. Rep.* **2021**, *11*, 5211. [CrossRef] [PubMed]
32. Coehoorn, R.; Haas, C.; Dijkstra, J.; Flipse, C.J.F.; de Groot, R.A.; Wold, A. Electronic structure of $MoSe_2$, MoS_2, and WSe_2. I. Band-structure calculations and photoelectron spectroscopy. *Phys. Rev. B* **1987**, *35*, 6195–6202. [CrossRef]

33. Perea-López, N.; Elías, A.L.; Berkdemir, A.; Castro-Beltran, A.; Gutiérrez, H.R.; Feng, S.; Lv, R.; Hayashi, T.; López-Urías, F.; Ghosh, S. Photosensor device based on few-layered WS2 films. *Adv. Funct. Mater.* **2013**, *23*, 5511–5517. [CrossRef]
34. Berkdemir, A.; Gutiérrez, H.R.; Botello-Méndez, A.R.; Perea-López, N.; Elías, A.L.; Chia, C.-I.; Wang, B.; Crespi, V.H.; López-Urías, F.; Charlier, J.-C. Identification of individual and few layers of WS2 using Raman Spectroscopy. *Sci. Rep.* **2013**, *3*, 1755. [CrossRef]
35. Cesano, F.; Bertarione, S.; Piovano, A.; Agostini, G.; Rahman, M.M.; Groppo, E.; Bonino, F.; Scarano, D.; Lamberti, C.; Bordiga, S.; et al. Model oxide supported MoS2 HDS catalysts: Structure and surface properties. *Catal. Sci. Technol.* **2011**, *1*, 123–136. [CrossRef]
36. Gutiérrez, H.R.; Perea-López, N.; Elías, A.L.; Berkdemir, A.; Wang, B.; Lv, R.; López-Urías, F.; Crespi, V.H.; Terrones, H.; Terrones, M. Extraordinary room-temperature photoluminescence in triangular WS2 monolayers. *Nano Lett.* **2013**, *13*, 3447–3454. [CrossRef] [PubMed]
37. Bhat, K.S.; Nagaraja, H. Effect of isoelectronic tungsten doping on molybdenum selenide nanostructures and their graphene hybrids for supercapacitors. *Electrochim. Acta* **2019**, *302*, 459–471. [CrossRef]
38. Wu, X.; Li, H.; Yang, X.; Wang, X.; Miao, Z.; Zhou, P.; Zhao, J.; Zhou, J.; Zhuo, S. Reduced Graphene Oxide Hydrogel for High Energy Density Symmetric Supercapacitor with High Operation Potential in Aqueous Electrolyte. *ChemElectroChem* **2021**, *8*, 4353–4359. [CrossRef]
39. Zhu, C.; Liu, T.; Qian, F.; Han, T.Y.-J.; Duoss, E.B.; Kuntz, J.D.; Spadaccini, C.M.; Worsley, M.A.; Li, Y. Supercapacitors Based on Three-Dimensional Hierarchical Graphene Aerogels with Periodic Macropores. *Nano Lett.* **2016**, *16*, 3448–3456. [CrossRef]
40. Meng, X.; Lu, L.; Sun, C. Green synthesis of three-dimensional MnO2/graphene hydrogel composites as a high-performance electrode material for supercapacitors. *ACS Appl. Mater. Interfaces* **2018**, *10*, 16474–16481. [CrossRef]
41. Kang, S.H.; Lee, G.Y.; Lim, J.; Kim, S.O. CNT–rGO Hydrogel-Integrated Fabric Composite Synthesized via an Interfacial Gelation Process for Wearable Supercapacitor Electrodes. *ACS Omega* **2021**, *6*, 19578–19585. [CrossRef] [PubMed]
42. Chi, H.Z.; Wu, Y.Q.; Shen, Y.K.; Zhang, C.; Xiong, Q.; Qin, H. Electrodepositing manganese oxide into a graphene hydrogel to fabricate an asymmetric supercapacitor. *Electrochim. Acta* **2018**, *289*, 158–167. [CrossRef]
43. Marcano, D.C.; Kosynkin, D.V.; Berlin, J.M.; Sinitskii, A.; Sun, Z.; Slesarev, A.; Alemany, L.B.; Lu, W.; Tour, J.M. Improved synthesis of graphene oxide. *ACS Nano* **2010**, *4*, 4806–4814. [CrossRef] [PubMed]
44. Tian, Q.; Li, N.; Liu, J.; Wang, M.; Deng, J.; Zhou, J.; Ma, Q. Catalytic hydrogenation of alkali lignin to bio-oil using fullerene-like vanadium sulfide. *Energy Fuels* **2015**, *29*, 255–261. [CrossRef]
45. Gong, Y.; Li, D.; Fu, Q.; Pan, C. Influence of graphene microstructures on electrochemical performance for supercapacitors. *Prog. Nat. Sci.* **2015**, *25*, 379–385. [CrossRef]
46. Khataee, A.; Eghbali, P.; Irani-Nezhad, M.H.; Hassani, A. Sonochemical synthesis of WS2 nanosheets and its application in sonocatalytic removal of organic dyes from water solution. *Ultrason. Sonochemistry* **2018**, *48*, 329–339. [CrossRef]
47. Vattikuti, S.V.P.; Nagajyothi, P.C.; Devarayapalli, K.C.; Shim, J. Depositing reduced graphene oxide onto tungsten disulfide nanosheets via microwave irradiation: Confirmation of four-electron transfer-assisted oxygen reduction and methanol oxidation reaction. *New J. Chem.* **2020**, *44*, 10638–10647. [CrossRef]
48. Zhang, Y.; Zhang, N.; Tang, Z.-R.; Xu, Y.-J. Graphene Transforms Wide Band Gap ZnS to a Visible Light Photocatalyst. The New Role of Graphene as a Macromolecular Photosensitizer. *ACS Nano* **2012**, *6*, 9777–9789. [CrossRef] [PubMed]
49. Xu, J.; Zhu, Y.; Yu, B.; Fang, C.; Zhang, J. Metallic 1T-VS_2 nanosheets featuring V^{2+} self-doping and mesopores towards an efficient hydrogen evolution reaction. *Inorg. Chem. Front.* **2019**, *6*, 3510–3517. [CrossRef]
50. Fang, W.; Zhao, H.; Xie, Y.; Fang, J.; Xu, J.; Chen, Z. Facile hydrothermal synthesis of VS2/graphene nanocomposites with superior high-rate capability as lithium-ion battery cathodes. *ACS Appl. Mater. Interfaces* **2015**, *7*, 13044–13052. [CrossRef] [PubMed]
51. Feng, J.; Sun, X.; Wu, C.; Peng, L.; Lin, C.; Hu, S.; Yang, J.; Xie, Y. Metallic Few-Layered VS_2 Ultrathin Nanosheets: High Two-Dimensional Conductivity for In-Plane Supercapacitors. *J. Am. Chem. Soc.* **2011**, *133*, 17832–17838. [CrossRef] [PubMed]
52. Sengupta, S.; Kundu, M. Carbon Free Nanostructured Plate like WS_2 with Excellent Lithium Storage Properties. *ChemistrySelect* **2020**, *5*, 14183–14189. [CrossRef]
53. Zhang, H.; Xie, A.; Wang, C.; Wang, H.; Shen, Y.; Tian, X. Bifunctional reduced graphene oxide/V2O5 composite hydrogel: Fabrication, high performance as electromagnetic wave absorbent and supercapacitor. *ChemPhysChem* **2014**, *15*, 366–373. [CrossRef]
54. Zhang, S.; Pan, N. Supercapacitors Performance Evaluation. *Adv. Energy Mater.* **2014**, *5*, 1401401. [CrossRef]
55. Ratha, S.; Rout, C.S. Supercapacitor electrodes based on layered tungsten disulfide-reduced graphene oxide hybrids synthesized by a facile hydrothermal method. *ACS Appl. Mater. Interfaces* **2013**, *5*, 11427–11433. [CrossRef] [PubMed]
56. Huang, Q.; Wang, J.; Liu, F.; Chang, X.; Chen, H.; Lin, H.; Han, S. Graphene-constructed flower-like porous $Co(OH)_2$ with tunable hierarchical morphologies for supercapacitors. *RSC Adv.* **2016**, *6*, 16745–16750. [CrossRef]